Dalton Transactions

ROYAL SOCIETY OF CHEMISTRY

PAPER

View Article Online
View Journal | View Issue

Cite this: *Dalton Trans.*, 2025, **54**, 6081

Conformational isomerization in $Co(acac)_2$ *via* spin-state switch: a computational study†

Shalini Joshi,[a] Sabyasachi Roy Chowdhury[a,b] and Sabyashachi Mishra *[a]

Received 8th January 2025,
Accepted 4th March 2025

DOI: 10.1039/d5dt00052a

rsc.li/dalton

Conformational dynamics of ligands in transition metal complexes can give rise to interesting physical, chemical, spectroscopic, and magnetic properties of the complexes. The changing ligand environment often affects the d-orbital splitting pattern that allows multiple possible ways of electron arrangement in the frontier molecular orbitals, resulting in several closely spaced electronic states with different orbital and spin symmetries. The system can explore these states with either thermal or photophysical means. In the present work, we demonstrate the possibility of a spin transition in $Co(acac)_2$ assisted by a conformational rearrangement of the ligand. Electronic structure calculations show that the complex adopts a square-planar and tetrahedral geometry with low-spin and high-spin electronic configurations, respectively. A spin-conserved conformational change involves a larger energy barrier in both high- and low-spin states. On the other hand, a low-lying minimum-energy-crossing point exists between the two spin-states that provides a low-energy pathway for conformational isomerization between the two isomers. While the spin-assisted isomerization from a tetrahedral to square planar form requires crossing a 10 kcal mol^{-1} barrier, the reverse barrier is only 2 kcal mol^{-1}. The calculation of the magnetic properties of the complex reveals a large magnetic anisotropy barrier of 57.6 cm^{-1} for this complex in the high-spin state.

1. Introduction

The spin-crossover (SCO) describes a phenomenon where a molecule alters its ground spin state triggered by external stimuli, such as temperature, pressure, light irradiation, or external electric and magnetic fields.[1–4] Since Cambi's pioneering discovery of the SCO effect in the tris(dithiocarbamato)Fe(III) complex,[5] it has become a well-known characteristic of the first-row transition metal ions with d^4 to d^7 electron configurations. These metal ions are often paired with ligands characterized by intermediate field strength, primarily N- and O-donors, which provide labile electronic configurations for the metal-complexes.[2,6–9]

While a considerable amount of research exists for iron-based SCO complexes,[4,8,10–13] exploration of Co(II) based SCO systems is rather limited.[2,14–17] The most commonly studied hexa-coordinated Co(II) complexes involve either an N_6 or an N_4O_2 coordination sphere, achieved through a combination of monodentate and chelating ligands. SCO in Co(II) complexes was initially observed in complexes with a $[CoN_6]^{2+}$ core where an intermediate magnetic moment at room temperature was reported.[18,19] Since then, N_6 based ligands, *e.g.*, the tridentate 2,2′;6′,2″-terpyridine (terpy) ligand and its numerous derivatives have proven highly effective in constructing Co(II) based SCO complexes.[20–22] Complexes with N_4O_2 coordination spheres include Co(II)-semiquinone compounds that demonstrate valence tautomerism,[14,23,24] and the well-studied quadridentate salen-type Schiff base Co(II) complexes have also been reported for their SCO behaviour.[19,25,26]

The spin-state switch is typically associated with a change in metal–ligand bond distances, arising from the changes in the electronic population of the metal–ligand bonding and anti-bonding orbitals.[27,28] However, there are instances where spin-state transition accompanies conformational isomerization in metal complexes.[19,29–31] The four-coordinated metal β-ketomine based complexes are a prime example, where the spin-state switch involves square-planar to tetrahedral isomerization, characterized by spectral, magnetic, and NMR methods.[29] This conformational isomerism has been observed in several bis-chelate complexes, especially those with α,β-unsaturated β-ketoamines.[32–35] Similarly, the $[Co(PEt_3)_2(NCS)_2]$ complex exhibits a transition from a tetrahedral to a dimeric-pyramidal conformation as it switches from high-spin (HS) to low-spin (LS) states.[36] Monomeric bis-

[a]*Department of Chemistry, Indian Institute of Technology Kharagpur, Kharagpur, India. E-mail: mishra@chem.iitkgp.ac.in*
[b]*Department of Chemistry, University of South Dakota, Vermillion, South Dakota, USA*

†Electronic supplementary information (ESI) available: Additional tables and figures. The coordinates of the optimized geometries. See DOI: https://doi.org/10.1039/d5dt00052a

chelate Co(II) complexes, such as [Co(SDPM)$_2$] (with SDPM: 2,2′,6,6′-tetramethyl-5-mercaptohept-4-en-2-one), also show the transition between planar and tetrahedral conformations.[30] Additionally, Co(II) triazene 1-oxide bis(chelates) complexes, such as [Co(OMeN$_3$C$_6$H$_4$Me-4)$_2$], demonstrate a planar to tetrahedral transition in solvents that do not coordinate with the metal ion.[31]

Among the metal bis-acetylacetonate (acac) complexes, the five-coordinated [Ni(acac)$_2$(pyridine)] complex is known to exist in three polytopal forms (a square-pyramid and two distinct trigonal bipyramids), separated by low-energy barriers.[37] Bis-chelate bis-(propane-1,3-dionato)Ni(II) and bis-(*N*-methyloxyvinylaldiminato)Ni(II) complexes have been studied computationally to elucidate the isomerization between the square-planar to tetrahedral forms and the role of spin states in governing the transition.[38] [Mg(acac)$_2$] is also known to exhibit square-planar and tetrahedral forms, although the involvement of the spin-state in its isomerism is unlikely.[39]

On the other hand, the structural and electronic characterization of Co(acac)$_2$ has been contentious and remains a topic of ongoing debate. Although the initial study of Cotton and Holm suggested a square-planar geometry,[40] the later studies show overwhelming evidence for a tetrahedral structure of Co(acac)$_2$ at room temperature.[41–44] From molecular weight measurements and visible- and near-infrared spectroscopy, it was found that tetrahedral Co(acac)$_2$ units oligomerise in non-coordinating solvents.[41] In dilute solutions, the compound predominantly adopts a mononuclear tetrahedral configuration, but at higher concentrations, it shows octahedral coordination due to additional interactions with diketonate oxygen atoms from adjacent units.[41] UV-visible-NIR spectroscopy lends further support to the tetrahedral Co(acac)$_2$ monomer, as reflected in the comparable spectra of Co(DPM)$_2$ (DPM: dipivaloylmethanido).[41] Later on, the X-ray crystal structure confirmed a tetrahedral geometry of the Co(acac)$_2$ monomer in a tetrameric assembly.[42,43] In 2000, Burgess *et al.* reported a square planar crystal structure for Co(acac)$_2$.[45] However, a later study in 2010 suggested this complex to be of copper instead of cobalt.[44,46] A square-planar arrangement of Co(acac)$_2$ is reported in coordinating solvents, where two solvent molecules occupy the two axial sites of the metal ion.[44] Temperature-dependent EPR study shows a HS ground state for Co(acac)$_2$L$_2$ (L = water and ethanol) below 40 K,[47] which is also supported by theoretical studies.[48] The computational modelling of the L$_{2,3}$-edge X-ray absorption spectra of the Co(acac)$_2$ complex confirms the contribution from both the HS and LS states.[49]

While the previous experimental and theoretical studies have focused on characterizing the ground spin-states and the relative stabilities of the square-planar and tetrahedral geometries of the Co(acac)$_2$ complex, the mechanism underlying their interconversion has remained unexplored. In this study, we elucidate the potential switching mechanism between these two geometries and examine the influence of spin-states on this process. Additionally, we investigate the magnetic anisotropy related to the two ground spin-states and explore the mechanisms governing the relaxation of magnetization.

2. Results and discussion

2.1. Molecular geometry analysis

Molecular geometry optimizations with density functional theory (DFT) methods show that the Co(acac)$_2$ complex adopts a tetrahedral-like geometry in the HS state (^{4}TD) and a square-planar like geometry in the LS state (^{2}SQP), Fig. 1. The $\langle S^2 \rangle$ values were used to examine the spin-contamination associated with the DFT calculations. For the ^{4}TD systems, all the functionals produced $\langle S^2 \rangle$ values between 3.76 and 3.77 (theoretical value 3.75). For the ^{2}SQP system, the $\langle S^2 \rangle$ values computed by TPSSh-D3, B3PW91-D3, and M05-D3 (0.77, 0.81, and 0.88, respectively) deviated marginally from the ideal value (0.76), while the rest of the functionals showed no spin-contamination ($\langle S^2 \rangle$ = 0.76) (see Table S1 in the ESI†). To understand the effect of dispersion correction on the optimized geometry, the molecular geometries and spin-splitting energies of both the ^{4}TD and ^{2}SQP complexes were also examined with and without considering the dispersion interaction. Using B3LYP and CAM-B3LYP functionals (with def2-TZVP basis), we find that the dispersion correction with either the B3LYP or CAM-B3LYP functional has a negligible effect on the geometry, as evident from the near-zero RMSD values (Table S2 in the ESI†).

The Co–O distances are found to vary between 1.93 and 1.95 Å in the ^{4}TD state optimized with different functionals employed together with the def2-TZVP basis set. This is consistent with the Co–O bond distances observed in the experimental geometry.[42–44] All bond parameters of the complexes are provided in Table S3 in the ESI.† In the optimized geometries of ^{4}TD, the two O–Co–O bite angles are around 94.9° and the two exterior O–Co–O angles are around 117.2°, deviating from the ideal tetrahedral value of 109.5°. On the other hand, in the ^{2}SQP geometry, the O–Co–O angles deviate by ±5° from their ideal value of 90°. Such deviations from the ideal bond angles are also consistent with the shape analysis.[50] Since the deviations in the angles are more pronounced in the ^{4}TD geometry, a shape deviation parameter of 1.6 is obtained for ^{4}TD,

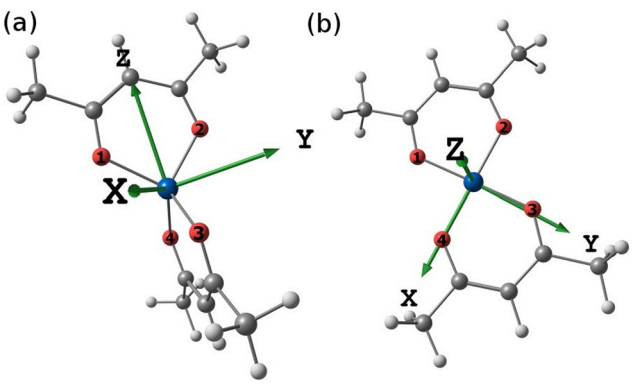

Fig. 1 The optimized geometries of Co(acac)$_2$ with (a) a tetrahedral structure in the HS state (^{4}TD) and (b) a square-planar structure in the LS state (^{2}SQP). Atom colour: Co in blue, O in red, C in grey, and H in white. The four coordinating oxygen atoms are numbered.

as compared to 0.09 for the ^{2}SQP geometry (see Table S3 in the ESI†). In the ^{2}SQP geometry, comparatively shorter Co–O bond distances (1.85–1.89 Å) are observed. Therefore, the spin-transition from ^{4}TD to the ^{2}SQP state not only influences the mode of coordination but is also associated with the reduction in the Co–O distances. The 3d-based MOs for the HS geometry, involve e-like ($3d_{x^2-y^2}$ and $3d_{z^2}$) and t_2-like ($3d_{xy}$, $3d_{yz}$, and $3d_{xz}$) orbitals (Fig. 2). In the TD geometry, ligands occupy alternating corners of a cube relative to the metal atom at the centre, and the $d_{x^2-y^2}$ and d_{z^2} orbitals (referred to as the e-orbitals) are lower in energy, as their lobes point between the ligand directions. The d_{xy}, d_{yz}, and d_{xz} (t_2 orbitals) are higher in energy due to their lobes being closer to the ligand axes. For the LS state in a square-planar geometry, the orbitals are identified as e_g ($3d_{xz}$, $3d_{yz}$), a_{1g} ($3d_{z^2}$), b_{2g} ($3d_{xy}$), and b_{1g} ($3d_{x^2-y^2}$). In the SQP geometry, the ligands lie in the *xy* plane, with the *z*-axis perpendicular to the ligand plane. The $d_{x^2-y^2}$ has the highest energy due to the strong interaction with the four planar ligands. The d-orbitals in the ^{4}TD and ^{2}SQP geometries are designated according to their idealized symmetry. The loss of orbital degeneracy in the HS state geometry indicates the deviation from an ideal tetrahedral geometry. In the LS state, the antibonding $d_{x^2-y^2}$ orbital carries no electrons (Fig. 2), thus shortening the metal–ligand bond length in the ^{2}SQP state as compared to the ^{4}TD state, where all d-orbitals are singly or doubly occupied.

2.2. Adiabatic energy differences

We employed four basis sets (def2-SVP, 6-311G(d,p), def2-TZVP, and def2-TZVPP) with the B3LYP-D3 functional and compared the geometry and adiabatic energy. The size of the basis sets was observed to have a minimal influence on the geometries of the complex (see Table S4†), although it affected the adiabatic energies of the HS and LS states. With the def2-SVP basis set (consisting of 297 basis functions), the computed energy difference is 11.9 kcal mol^{-1}. This value decreases to 7.6 kcal mol^{-1} with the 6-311G(d,p) basis set (382 basis functions). Conversely, computation with def2-TZVPP (with 694 basis functions) yielded an energy difference of 8.9 kcal mol^{-1}, very close to the value calculated with the def2-TZVP (with 563 basis functions) basis set (8.6 kcal mol^{-1}). Based on the observed convergence (Table S5 in the ESI†) of the adiabatic energy difference with the def2-TZVP basis set, we carried out all other DFT calculations using this basis set.

While different DFT functionals resulted in very similar optimized geometries, the spin-splitting energies are found to vary substantially with different functionals, as observed in several other systems.[51–53] Pure DFT functionals BP86-D3 and BLYP-D3 suggest a more stable ^{2}SQP geometry compared to the ^{4}TD complex (Fig. 3 and Table S1 in the ESI†). Conversely, the hybrid DFT functionals estimate a more stable ^{4}TD state than the ^{2}SQP state. For instance, B3LYP*-D3 (having 15% Hartree–Fock (HF) exchange), B3LYP-D3 and B3PW91-D3 (both incorporating 20% HF exchange) suggest adiabatic spin-state energy differences of 10.3, 8.6 and 11.1 kcal mol^{-1}, respectively, between the LS and HS states. The range-separated CAM-B3LYP-D3 indicates an adiabatic energy difference of 11.9 kcal mol^{-1}, whereas the *meta*-hybrid-GGA functionals TPSSh-D3 (10% HF exchange), M05-D3 (28% HF exchange), and M06-D3 (27% HF exchange) predict energy differences of 7.0, 13.3 and 4.7 kcal mol^{-1}, respectively. The B2PLYP optimization was found to be very expensive. Instead, we performed single-point energy calculation with B2PLYP/def2-TZVP (using the B3LYP-D3/def2-TZVP optimized geometry). This is justified since the optimized geometry shows negligible dependence on functional, basis set, and dispersion correction. The double-hybrid B2PLYP estimates a significantly larger spin-splitting energy (31.5–33.9 kcal mol^{-1}) as compared to the other functionals (see Table S6 in the ESI†). Employing the complete active space second-order perturbation theory (CASPT2) method, Radoń *et al.* have estimated this energy difference to be 13 kcal mol^{-1}.[48] Although hybrid functionals with 10–15%

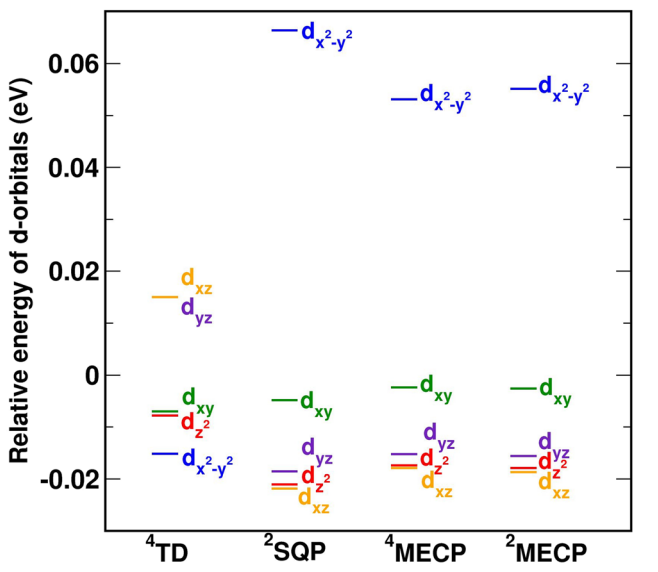

Fig. 2 The d-orbital energy levels of Co(acac)$_2$ at the optimized geometry in the HS state (^{4}TD), in the LS state (^{2}SQP), and at the minimum-energy cross point between the HS and LS states in the LS configuration (^{2}MECP) and HS configuration (^{4}MECP). The orbital energy levels are shown with respect to the corresponding barycentre.

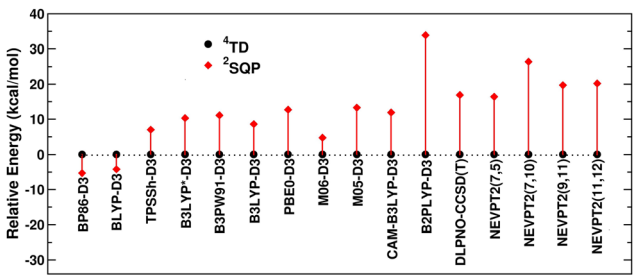

Fig. 3 The energy of the square-planar Co(acac)$_2$ in the LS (^{2}SQP) state, as compared to that of the tetrahedral geometry in the HS state (^{4}TD), obtained from different DFT functionals, and using DLPNO-CCSD(T) and NEVPT2 methods.

Hartree–Fock (HF) exchange have been shown to provide the best estimates of spin-splitting energies, their accuracy varies from system to system.[54,55] Such deviation in the spin-splitting energies across various functionals is previously noted.[52] The dispersion correction lowers the spin-splitting energy by ~2 kcal mol^{-1} with the B3LYP functional, while with the CAM-B3LYP functional, it shows a small change of 0.4 kcal mol^{-1}. The range-separated functional CAM-B3LYP includes the correction terms for the long-range interactions. Hence, the dispersion correction has a marginal contribution to the geometry and energy with CAM-B3LYP (see Table S2 in the ESI†).

The significant variation in the adiabatic energy differences (−5.3 to 13.3 kcal mol^{-1}) calculated with different DFT functionals prompted us to conduct a further comparison with the domain-based local pair natural orbital coupled cluster method (DLPNO-CCSD(T)). While CCSD(T) is widely acknowledged as the "gold standard" for electron correlation recovery in single-reference methods, its application is limited to relatively small systems.[56–61] The recent development of the domain-based local pair natural orbital coupled cluster method (DLPNO-CCSD(T)) allows larger systems to be studied with near DFT speed and near CCSD(T) accuracy.[56,57,62–64] Therefore, we compared the DFT-computed adiabatic energy difference between the ^{4}TD and ^{2}SQP complexes with those obtained from the DLPNO-CCSD(T) method. The DLPNO-CCSD(T) computed energy difference is 16.9 kcal mol^{-1}, higher than those generated by pure, hybrid DFT functionals, reparametrized hybrid functionals, and hybrid *meta*-GGA functionals (Table S1†). However, the DLPNO-CCSD(T) method preserves the trend seen with the hybrid DFT functionals, *i.e.*, the ^{4}TD state is more stable than the ^{2}SQP state. We opted to utilize the B3LYP-D3/def2-TZVP method for the geometry calculations and subject the molecular geometries to high-level wavefunction theory methods to evaluate the energetics and other observables. The B3LYP functional has also been used in other computational work on Co(II) complexes.[47,49,65]

The impact of non-coordinating solvents was investigated by optimizing the complex with B3LYP-D3/def2-TZVP in benzene and toluene solvents with a PCM model. An energy difference of ±1 kcal mol^{-1} was observed between the gas phase and solvent energetics (see Table S7†). The relativistic effect is also analysed using PBE0, TPSSh, and B3LYP functionals (Table S8 in the ESI†). A negligible change in the energy is found with the DKH/ZORA scalar relativistic effect. The energy difference with and without relativistic corrections is within 1 kcal mol^{-1}, in agreement with the observation in other 3d-metal complexes.[66]

The energy difference between the two spin-states is also determined by the multireference methods by using (7,5) and (7,10) active spaces. In the first-row transition-metal complexes, efficient treatment of electron correlation in a multiconfiguration framework requires a second set of nd-orbitals to model chemical bonding[67] and energetics,[68] known as the "double d-shell effect".[69] The lowest spin-free energies of the HS and LS geometries (with one quartet and three doublet roots) using (7,5) and (7,10) active spaces for the $Co(acac)_2$ complex are provided in Table S9 of the ESI.† There is not much difference in energetics with the two active spaces when computed with the complete active space self-consistent field (CASSCF) method. However, when dynamical electron correlation is included by employing the N-electron valence state perturbation theory (NEVPT2), a significant change in energy is observed in (7,5) and (7,10) active spaces for both the ^{4}TD and ^{2}SQP conformers, justifying the use of double d-shells in d^7 systems. Furthermore, we considered two additional active spaces that include ligand orbitals in addition to the five 3d-orbitals and the five double d-shell orbitals. By including one and two ligand orbitals, we get (9,11) and (11,12) active spaces, respectively (Fig. S9 to S12 in the ESI†). The spin-state energy gap from the (9,11) active space shows a significant difference from that of the (7,10) active space at CASSCF, NEVPT2, and quasi-degenerate (QD)-NEVPT2 level of theories. Including the second ligand orbital (*i.e.*, (11,12)) changes the spin-state gap marginally (Table S9 in the ESI† and Fig. 3). For all active spaces, NEVPT2 and QD-NEVPT2 yield very similar results (Table S9 in the ESI†).

2.3. Mechanism of spin-state switching

To assess how the mode of ligand coordination impacts the relative stability of the spin-states, we conducted a one-dimensional potential energy scan along the dihedral plane of the four oxygen atoms coordinated to the metal ion. This dihedral angle connects the ^{4}TD geometry to the ^{2}SQP geometry (Fig. 4). The doublet state lies 32 kcal mol^{-1} above the quartet at the tetrahedral geometry. As we progress towards the square planar geometry by altering the dihedral angle, the energy of

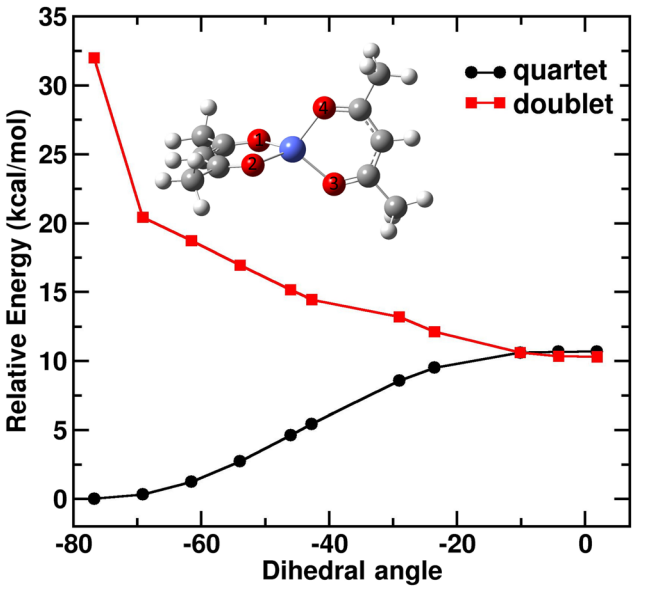

Fig. 4 The one-dimensional potential energy scan of the ^{4}TD and ^{2}SQP states along the rotation of the dihedral angle (1, 2, 3 and 4 highlighted in the inset) using the B3LYP-D3/def2-TZVP method.

the quartet state gradually rises while the doublet state gets stabilized (Fig. 4). Notably, at a dihedral angle of approximately −10° (nearing a square planar geometry), the two spin-states intersect (see Fig. 4). At the square-planar geometry, the ^{2}SQP state appears <1 kcal mol^{-1} below the ^{4}TD state. The one-dimensional dihedral scan shows how the doublet and quartet states change their energy and provides insight into the transition structure along the quartet and doublet potential energy curves. In a non-coordinating solvent medium (benzene), the potential-energy profile along this dihedral angle follows a similar pattern (Fig. S1 in the ESI†). The presence of the solvent reduces the spin-splitting energy, resulting in a decrease of 2 kcal mol^{-1} in the crossing energy compared to the gas-phase crossing point (see Fig. S1 in the ESI†).

A transition state (TS) search was carried out (with the B3LYP-D3/def2-TZVP method) in the HS electronic configuration that connects two equivalent forms of the tetrahedral geometry (^{4}TD and ^{4}TD′, which can be generated by a 180° rotation along the dihedral angle formed by the four oxygen centres coordinated to Co). The transition state (TS1) exhibits a four-coordinate square-planar geometry, with all the O–Co–O angles approximating 90° and all Co–O bond lengths elongated (1.99 Å) relative to the ^{2}SQP structure (Table S12†). TS1 has an activation energy barrier of 11 kcal mol^{-1} (see Fig. 5 and Table S13†). It is characterized by a single imaginary vibrational mode with a frequency of −21 cm^{-1} (Table S14 and Fig. S2†). Similarly, within the doublet spin multiplicity, the transition state search yielded a four-coordinated distorted tetrahedral structure (TS2) that connects two equivalent forms of the square-planar geometry (^{2}SQP and ^{2}SQP′). The TS2 has Co–O bond lengths ranging from 1.91 Å to 1.96 Å and O–Co–O angles varying from 93° to 124° (see Table S12†). TS2 has an activation energy barrier of 13 kcal mol^{-1} and is associated with a single imaginary vibrational mode with a frequency of −123 cm^{-1} (see Fig. 5, and Table S13†). The transition states are also confirmed by IRC calculations (Fig. S4†).

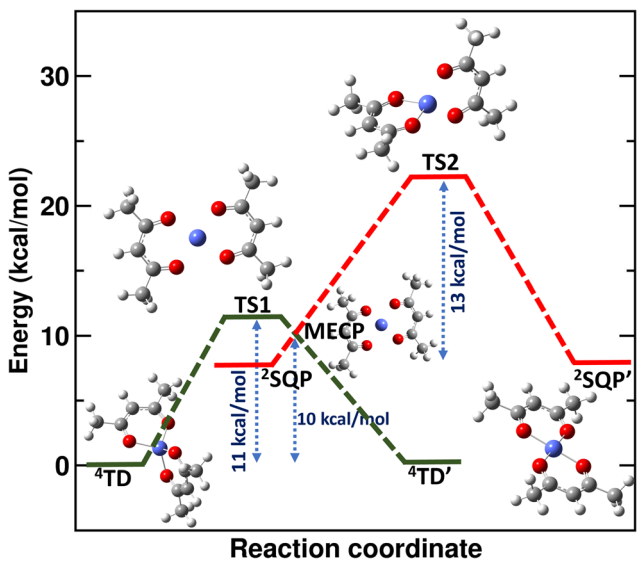

Fig. 5 Schematic energy diagram of spin-state switching in Co(acac)$_2$. ^{4}TD and ^{4}TD′ correspond to minima in the quartet PE curve, and ^{2}SQP and ^{2}SQP′ are the minima in the doublet PE curve. TS1 and TS2 represent the transition states along the quartet and doublet PE curves, respectively. MCEP indicates the minimum energy crossing point between the HS and LS curves.

Investigation of the potential energy (PE) surfaces in both spin manifolds suggests that the molecular orientation in the ^{4}TD and ^{2}SQP geometries is entirely governed by the spin state. As a result, we did not observe any square-planar minimum in the quartet PE profile or the tetrahedral minimum in the doublet PE profile. Instead of finding a pathway for conformational transition within a particular spin-state, we tried to find a pathway that involves a change in the spin-state. To that end, the minimum energy crossing point (MECP) between the HS and LS state was optimized using the B3LYP-D3/def2-TZVP method.

The computed MECP represents the minimum energy geometry where the ^{4}TD and ^{2}SQP states are degenerate, and the spin transition from ^{4}TD to ^{2}SQP can occur through this critical point. The optimized MECP results in a structure reminiscent of the square-planar geometry with elongated Co–O bonds. The Co–O bond length and the angles O_2–Co–O_3, O_4–Co–O_1 in the MECP structure acquire values in between the corresponding values in the ^{4}TD and ^{2}SQP geometries. The d-orbital energy levels at the MECP structure (Fig. 2, Table S10†) show a similar d-orbital energy ordering in both HS and LS electronic configurations. In the MECP geometry, the ligands lie in the *xy*-plane, with the *z*-axis perpendicular to the ligand plane. The reduced gap between the antibonding $d_{x^2-y^2}$ and the rest of the d-orbitals in the MECP geometry indicates a reduced energy gap between the HS and LS states. The energy (electronic energy with zero-point energy correction) and bond parameters of all the structures are given in Tables S12 and S13,† respectively. The calculated MECP is 10.3 kcal mol^{-1} above the ^{4}TD state and 1.7 kcal mol^{-1} higher than the ^{2}SQP geometry. In Fig. 5, a schematic diagram shows different pathways for conformational transition. Since the ^{2}SQP state lies about 8.6 kcal mol^{-1} above the ^{4}TD state, its equilibrium population is expected to be low from a thermodynamic point of view. It is clear that the spin-assisted conformational transition involves a comparatively smaller barrier. In particular, a very small barrier between the ^{2}SQP state and the MECP (<2 kcal mol^{-1}) indicates the possibility of a spontaneous conformational transition from a square-planar to a tetrahedral structure. However, the tetrahedral to square-planar conformational transition involves a barrier inaccessible through thermal means. This explains the lack of structural evidence of square-planar Co(acac)$_2$, despite several attempts.[40,44–46]

2.4. Magnetic properties of the Co(acac)$_2$ complexes

Pietrzyk and co-workers investigated the magnetic properties of the Co(acac)$_2$ complexes by EPR measurements.[47] From the unresolved EPR spectra, the zero-field splitting (ZFS) parameters could not be experimentally measured. Consequently, the spin-Hamiltonian parameters were computed using the

DFT method. The magnetic properties involve excited electronic states of a molecule, where the multi-configuration interactions dominate. DFT is well known to fall short in describing such interactions. It further suffers from strong functional dependence in describing the sign and magnitude of the ZFS parameters.[52] Although the ground state energy can be reliably estimated from single-reference methods, such as DFT or DLPNO-CCSD(T), both ground and excited states, coupled *via* the spin–orbit operators, contribute to the magnetic properties of the complex. Hence, we have evaluated the magnetic parameters using the multi-configurational second-order perturbation theory methods. The spin–orbit coupling was treated *a posteriori*.

To explore the magnetic anisotropy of the $Co(acac)_2$ complex, we conducted state-averaged (SA)-CASSCF calculations on the molecular geometries optimized with the B3LYP-D3/def2-TZVP method. Our approach involved utilizing an active space of (7,5), representing seven metal d-electrons distributed across five 3d-orbitals. Additionally, the influence of the second d-shell was taken into account by incorporating the five 4d-orbitals into an active space of (7,10). Since the CASSCF method takes into account only the static electron correlation, the dynamical electron correlation was evaluated by subjecting the SA-CASSCF wavefunctions to NEVPT2 calculations.

In the ^{4}TD geometry, the (7,5)-SA-CASSCF computed ground (Q_0) and the first excited quartet states (Q_1) are separated by 1898 cm^{-1}, which increases to 1985 cm^{-1}, when the (7,10) active space is used. The Q_2 and Q_3 states form a quasi-degenerate pair in both the active spaces. The energy differences between Q_0 and Q_2 states were estimated to be 5238 cm^{-1} with (7,5) and 5525 cm^{-1} with (7,10) active spaces. The SA-CASSCF energetics computed by the two active spaces are found to be consistent with each other. Including dynamical electron correlation increases the energy separation between the Q_0 and Q_1 states from 1985 cm^{-1} in (7,10) CASSCF to 2256.4 cm^{-1}. Similarly, the gap between the Q_0 and Q_2 states also increased to 6447.2 cm^{-1} (compared to 5237.8 cm^{-1} in CASSCF), while the near degeneracy of the Q_2 and Q_3 states is maintained. Conversely, in the ^{2}SQP geometry, the scalar-relativistic energy levels demonstrate significant sensitivity to the incorporation of the second d-shell and dynamical electron correlation (see Table 1). The gap between the lowest energy LS state and the first excited LS state (D_0 and D_1, respectively) decreases from 1503 cm^{-1} to 939 cm^{-1} when the double-d-shell effect is included in the (7,5)-SA-CASSCF. It decreases to 317 cm^{-1} upon accounting for the dynamic electron correlation through the NEVPT2 level of theory with the (7,10) active space.

The scalar-relativistic states computed by the SA-CASSCF/NEVPT2 methods are subjected to spin–orbit mixing, which results in Kramers doublets for the odd electron systems with $S > 1/2$. When a (7,5) active space is used for the SA-CASSCF/NEVPT2 calculations, the ground Kramers doublets are separated from the first excited Kramers pairs by 61.2 cm^{-1}, which shifts to 57.6 cm^{-1}, with the (7,10) active space. This separation gets marginally affected (within 2–4 cm^{-1}) in the presence of the energetically closed doublet states that are known to contribute to anisotropy by spin–flip excitations.[70] Analysis of the spin–orbit states suggests that the low-lying Kramers doublets are primarily composed of the non-degenerate Q_0 states, with marginal contribution from the Q_1 states, and this remains the same, irrespective of the choice of the active space for the SA-CASSCF/NEVPT2 calculations (see Table S16†).

Table 1 The energy (in cm^{-1}) of the lowest four spin-free and spin–orbit states of HS and LS conformers of the $Co(acac)_2$ complex with SA-CASSCF and NEVPT2 methods by using 10 quartet roots in the ^{4}TD geometry and 40 doublet roots in ^{2}SQP in different active spaces

	Spin-free states		Spin–orbit states	
State (active-space)	CASSCF	NEVPT2	CASSCF	NEVPT2
^{4}TD	0 (Q_0)	0 (Q_0)	0	0
CAS(7,5)	1898.2 (Q_1)	2256.4 (Q_1)	68.9	61.2
	5237.8 (Q_2)	6447.2 (Q_2)	1988.8	2337.2
	5240.2 (Q_3)	6450.1 (Q_3)	2145.2	2470.3
^{4}TD	0 (Q_0)	0 (Q_0)	0	0
CAS(7,10)	1984.7 (Q_1)	2170.2 (Q_1)	62.3	57.6
	5524.7 (Q_2)	5986.5 (Q_2)	2066.4	2245.8
	5527.2(Q_3)	5988.7 (Q_3)	2206.4	2375.4
^{2}SQP	0 (D_0)	0 (D_0)	0	0
CAS(7,5)	1503.4 (D_1)	170.5 (D_1)	1569.3	703.2
	2021.6 (D_2)	1420.2 (D_2)	2463.8	2031.0
	8595.1 (D_3)	9722.7 (D_3)	8761.0	10 104.1
^{2}SQP	0 (D_0)	0 (D_0)	0	0
CAS(7,10)	938.5 (D_1)	317.3 (D_1)	1104.9	734.4
	1625.6 (D_2)	1374.9 (D_2)	2125.9	1966.1
	8378.9 (D_3)	8592.5 (D_3)	8601.9	8931.9

The spin–orbit states are subjected to the SINGLE_ANISO module to evaluate the magnetic parameters, such as zero-field splitting (ZFS) parameters and *g*-tensors. For systems with unsaturated coordination numbers and unquenched angular momentum, spin–orbit coupling plays a significant role in governing the axial (D) and rhombic (E) ZFS parameters. The (7,5)-SA-CASSCF/NEVPT2/RASSI/SINGLE_ANISO calculation results $D = -30.6$ cm^{-1} and $E = -0.003$ cm^{-1}. A similar calculation with the (7,10) active space slightly lowers the magnitude of D to -28.8 cm^{-1}, although the E-value remains unchanged (Table S17†). The negative values of D and a small E/D ratio indicate easy-axis type anisotropy in the ^{4}TD of $Co(acac)_2$ and suggest the complex is a potential single-molecule magnet (SMM). The ZFS parameters are known to vary with the dihedral angle.[71,72] In $Co(acac)_2$, the HS state of the complex converts to the LS state with a dihedral change. Given that the ZFS parameters are not defined for the LS states ($S = 1/2$), the dihedral dependence of ZFS parameters is not explored in this work.

SMMs exhibit a preferential direction of magnetization, also known as "easy axis" and can retain magnetization for a considerable period of time. The *g*-tensors associated with the Kramers pairs indicate the preferential direction of magnetization in a particular spin–orbit state. The *g*-tensors were computed for pseudospin $S = 1/2$. According to the Kramers theorem, pseudospin $S = 1/2$ corresponds to Kramers doublets that remain degenerate in the absence of any applied magnetic

field and, hence, exhibit no ZFS.[73] While our computed axial ZFS parameter is consistent with that observed from DFT,[47] the magnitude of the *g*-tensors is different. While the DFT computations show isotropic *g*-tensors, our calculation shows for the ground spin–orbit pairs, the *g*-tensors are $g_x = g_y = 0$, and $g_z = 7.6$ (with both the active spaces), indicating the *Z*-axis as the preferential direction ("easy axis") of magnetization. On the other hand, in the first excited spin–orbit states, the magnitude of the *g*-tensors changes significantly. The increase in the magnitude of g_x and g_y to 4.3 and a simultaneous reduction of g_z to 2.6 suggest a decrease in the uniaxial magnetic anisotropy. Such changes in *g*-values are also accompanied by deviation in the magnetisation direction (Table S18†). Such non-coincidence of the excited-state anisotropy axis with respect to that of the ground Kramers doublet leads to fast relaxation of the magnetization.[74] To probe the mechanism of the relaxation of magnetization, we computed the transition-magnetic-moment matrix elements between the connecting pairs of spin–orbit states of the opposite magnetic moments (Fig. 6). The calculated transition-magnetic-moment matrix elements between the ground Kramers doublets are very small ($0.0005\mu_B$), suggesting a negligible quantum tunnelling of magnetization from the ground spin–orbit pairs. It is consistent with the uniaxial magnetic anisotropy predicted by the magnitudes of the *g*-tensors. Conversely, the higher transition magnetic moment matrix element between the first excited spin–orbit states ($1.45\mu_B$) suggests significant relaxation of magnetization. This is also consistent with the increase in the transverse components of the *g*-tensors ($g_x = g_y > g_z$) than the axial component in the first excited spin–orbit states. Such relaxation of magnetization from the first-excited spin–orbit pairs is known as thermally-assisted quantum tunnelling of magnetization (TA-QTM),

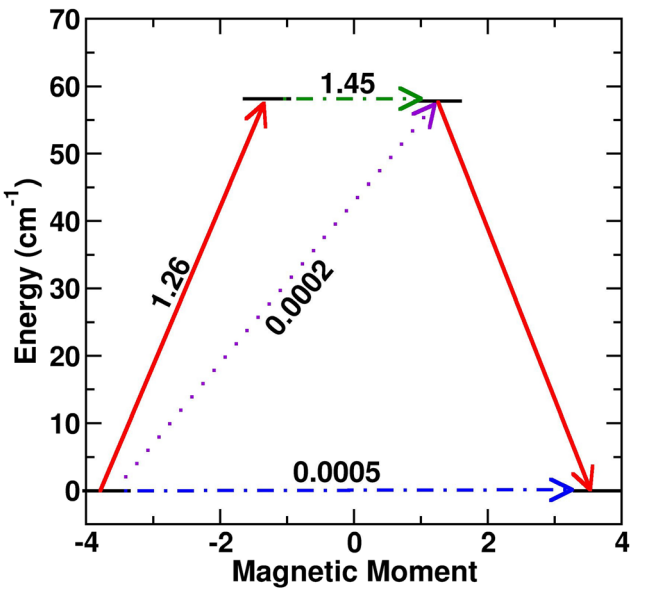

Fig. 6 The mechanism of relaxation of magnetization using CAS(7,10) in the ^{4}TD complex.

which results in an effective magnetic anisotropy barrier (U_{eff}) of 61.2 cm^{-1}, with the (7,5) active-space. The inclusion of the second d-shell marginally reduces the U_{eff} to 57.6 cm^{-1}. A large U_{eff} indicates the potential of $Co(acac)_2$ as a single-molecule magnet.

The anisotropic *g*-tensors and the negative axial ZFS parameter fit the criteria for a molecule to behave as a single-molecule magnet. Furthermore, the anisotropic *g*-tensors of the ground spin–orbit states are also consistent with the small relaxation of magnetization from the ground spin–orbit pairs. Reduction in the anisotropy in the first-excited spin–orbit pairs results in the relaxation of magnetization from the first-excited spin–orbit pairs by the TA-QTM process.

3. Computational details

The geometry optimization of the $Co(acac)_2$ complex at the HS and LS states was carried out using a number of DFT functionals, together with the def2-TZVP basis sets on all the elements.[75,76] Two pure DFT functionals BP86[77,78] and BLYP;[79] four hybrid DFT functionals B3PW91,[80,81] B3LYP,[79,82,83] PBE0,[84] and CAM-B3LYP;[85] one reparametrized hybrid functional B3LYP*;[86] three hybrid *meta*-GGA functionals TPSSh,[87] M05,[88] and M06;[89] and one double-hybrid functional B2PLYP[90] were employed. Grimme's D3 dispersion correction with the original damping function was used in all the geometry optimizations.[91,92] No symmetry restrictions were used. All the geometries were confirmed as minima using harmonic vibrational analysis. The absence of imaginary frequency confirms the stability of the computed molecular geometries in the respective spin states.

The potential energy scan was carried out in both HS and LS multiplicities along the dihedral angle that connects the tetrahedral structure with the square-planar structure. The transition state between the tetrahedral and square-planar structures was determined in the quartet and doublet potential energy surfaces. These transition state structures were confirmed through the imaginary frequencies and further validated through the intrinsic reaction coordinate (IRC) calculations that connect two correct minima. The crossing between the LS and HS potential-energy surfaces provides the first estimation of the crossing point between the two geometries. To evaluate the mechanism of spin-state switching and associated structural changes between the HS and LS states, a search for the minimum energy crossing point (MECP) was carried out by using a program developed by Harvey *et al.*,[93] where the location of the MECP is determined by employing a constrained optimization in both spin states.[94,95] All the optimization and frequency calculations described in this work were done using Gaussian 16 software.[96]

The adiabatic energy differences calculated using a series of DFT functionals were compared with those determined from DLPNO-CCSD(T) computations.[97–100] In the DLPNO-CCSD(T) calculations, B3LYP-computed unrestricted Kohn–Sham determinants served as the reference. The elements of the first

coordination sphere, Co and O atoms, were treated with the aug-cc-pwcvtz basis set,[101] and the remaining elements were treated with the cc-pvdz basis set.[101,102] The auxiliary basis sets (AuxJ, AuxC, and AuxJK) were generated using the "Autoaux" generation procedure.[103] The DLPNO-CCSD(T) method can fall short when the states are closely spaced and multireference interactions dominate.[104,105] However, the ability of the method to capture the dynamic correlation can be assessed from the so-called T_1 diagnostic.[106]

To evaluate the magnetic properties of the systems, the DFT-optimized geometries were subjected to the multi-configurational SA-CASSCF[107,108] followed by NEVPT2 calculations.[109–111] Dynamical correlation effects, which are not captured by the CASSCF method, are incorporated through the NEVPT2 and QD-NEVPT2 approaches.[112] The scalar-relativistic effects were treated using the Douglas–Kroll–Hess (DKH) Hamiltonian. For multireference calculations the DKH-def2-TZVP basis set was used for Co and O, and DKH-def2-SVP was used for C and H atoms. The auxiliary basis sets were generated by using the "Autoaux" procedure, as mentioned previously. The convergence criteria were set to be tighter than the default by choosing the "tightscf" option. For SA-CASSCF calculations, an active space of seven-d electrons in five 3d-orbitals (7,5) was used. The effect of the double d-shell was taken into account by accommodating another set of five d-orbitals, with (7,10) as the active space. Both the active spaces were used for state-averaged calculations of 10 quartet states and 40 doublet states. A comparison of energetics and magnetic parameters obtained from these two active spaces enables us to elucidate the role of the double d-shell in governing these properties. We also include the doubly occupied ligand orbitals into the active space, expanding it by accommodating one or two ligand-based orbitals along with five 3d- and 4d-atomic orbitals of the metal center, leading to (9,11) and (11,12) active spaces. The adiabatic separation energy between the ground quartet state of the ^{4}TD complex and the three-fold degenerate doublet ground state of the ^{2}SQP complex was obtained from these active spaces and was compared with those obtained from active spaces (7,5) and (7,10), different DFT functionals and the DLPNO-CCSD(T) method (Fig. 3). The energy levels of the d-orbitals were computed using *ab initio* ligand field theory (AILFT).[113,114] The scalar-relativistic states (10 quartets and 40 doublets) obtained by (7,5) or (7,10)-SA-CASSCF/NEVPT2 calculations were subjected to the RASSI module to evaluate the spin–orbit mixing of states.[115] The zero-field splitting (ZFS) parameters, *g*-tensors, and effective barrier of magnetic anisotropy (U_{eff}) were determined using the SINGLE_ANISO[116] module. All DLPNO-CCSD(T), CASSCF, NEVPT2, and QD-NEVPT2 calculations were performed using Orca 5.0.4 software.[117–119]

4. Conclusions

The geometry of $Co(acac)_2$ has been a contentious topic for several decades. In this study, we have examined the relative stability of the $Co(acac)_2$ complex in tetrahedral and square-planar geometries. The relative energy differences of the two geometries are computed with different DFT functionals and are further benchmarked against the DLPNO-CCSD(T) method. The hybrid functionals and DLPNO-CCSD(T) methods predict a stable tetrahedral geometry in a HS electronic configuration and a stable square-planar geometry in a LS configuration. Once the relative stabilities are characterized, the inter-conversion mechanism between the two conformers is explored. Our investigation shows that the conformational arrangement of the molecule in the tetrahedral and square-planar geometries is governed by a spin-state switch. The conformation change within a given spin-multiplicity (either quartet or doublet) involves a large barrier. On the other hand, when a spin-state switch is allowed, the complex finds a relatively low-lying minimum-energy-cross point between ^{4}TD and ^{2}SQP states. This crossing point lies 10 kcal mol^{-1} above the ^{4}TD state, while it is only 2 kcal mol^{-1} above the ^{2}SQP state, explaining why it has been difficult to isolate and characterize ^{2}SQP $Co(acac)_2$.[40,44–46] With multi-reference CASSCF/NEVPT2 methods together with spin–orbit coupling, the magnetic properties of the ^{4}TD state of $Co(acac)_2$ are examined. The effects of the double d-shell and dynamic electron correlation on the spin-state energetics, *g*-tensors, ZFS parameters, and magnetic anisotropy barrier are evaluated. Our investigation shows that in the ^{4}TD geometry, the ground spin–orbit state is magnetically anisotropic, and the molecule exhibits an anisotropy barrier of 57.6 cm^{-1}.

Data availability

The data supporting this article have been included as part of the ESI.†

Conflicts of interest

The authors declare no conflicts of interest.

Acknowledgements

SJ acknowledges the UGC, India, New Delhi, for the research fellowship. SRC acknowledges the support from IIT Kharagpur and the University of South Dakota. SM acknowledges the support from the SERB, DST, Government of India (CRG/2022/004088 and SR/FST/CSII-026/2013), and the CSIR, New Delhi, India (01(2987)/19/EMR-II). This work used the resources of the Paramshakti supercomputing facility of IIT Kharagpur and Paramporul supercomputing facility of NIT Trichy established under the National Supercomputing Mission of the Government of India and supported by CDAC, Pune.

References

1 S. Hayami, Z. Z. Gu, M. Shiro, Y. Einaga, A. Fujishima and O. Sato, First Observation of Light-Induced Excited Spin State Trapping for an Iron(III) Complex, *J. Am. Chem. Soc.*, 2000, **122**, 7126–7127.

2 S. Hayami, Y. Komatsu, T. Shimizu, H. Kamihata and Y. H. Lee, Spin-crossover in cobalt(II) compounds containing terpyridine and its derivatives, *Coord. Chem. Rev.*, 2011, **255**, 1981–1990.

3 S. Brooker, Spin crossover with thermal hysteresis: practicalities and lessons learnt, *Chem. Soc. Rev.*, 2015, **44**, 2880–2892.

4 R. W. Hogue, S. Singh and S. Brooker, Spin crossover in discrete polynuclear iron(II) complexes, *Chem. Soc. Rev.*, 2018, **47**, 7303–7338.

5 L. Cambi and L. Szegö, Über die magnetische Susceptibilität der komplexen Verbindungen, *Ber. Dtsch. Chem. Ges. B*, 1931, **64**, 2591–2598.

6 P. M. Becker, C. Förster, L. M. Carrella, P. Boden, D. Hunger, J. van Slageren, *et al.*, Spin Crossover and Long-Lived Excited States in a Reduced Molecular Ruby, *Chem. – Eur. J.*, 2020, **26**, 7199–7204.

7 Y. Chen, F. Cao, R. M. Wei, Y. Zhang, Y. Q. Zhang and Y. Song, Spin-crossover phenomena of the mononuclear MnIII complex tuned by metal dithiolene counteranions, *Dalton Trans.*, 2014, **43**, 3783–3791.

8 D. J. Harding, P. Harding and W. Phonsri, Spin crossover in iron(III) complexes, *Coord. Chem. Rev.*, 2016, **313**, 38–61.

9 B. Dey and V. Chandrasekhar, FeII spin crossover complexes containing N4O2 donor ligands, *Dalton Trans.*, 2022, **51**, 13995–14021.

10 J. Y. Ge, Z. Chen, L. Zhang, X. Liang, J. Su, M. Kurmoo, *et al.*, A Two-Dimensional Iron(II) Coordination Polymer with Synergetic Spin-Crossover and Luminescent Properties, *Angew. Chem., Int. Ed.*, 2019, **58**, 8789–8793.

11 H. S. Scott, R. W. Staniland and P. E. Kruger, Spin crossover in homoleptic Fe(II) imidazolylimine complexes, *Coord. Chem. Rev.*, 2018, **362**, 24–43.

12 H. L. Feltham, A. S. Barltrop and S. Brooker, Spin crossover in iron(II) complexes of 3, 4, 5-tri-substituted-1, 2, 4-triazole (Rdpt), 3, 5-di-substituted-1, 2, 4-triazolate (dpt -), and related ligands, *Coord. Chem. Rev.*, 2017, **344**, 26–53.

13 L. J. Kershaw Cook, R. Mohammed, G. Sherborne, T. D. Roberts, S. Alvarez and M. A. Halcrow, Spin state behavior of iron(II)/dipyrazolylpyridine complexes. New insights from crystallographic and solution measurements, *Coord. Chem. Rev.*, 2015, **289–290**, 2–12.

14 J. Olguín, Unusual metal centres/coordination spheres in spin crossover compounds, *Coord. Chem. Rev.*, 2020, **407**, 213148.

15 O. Drath and C. Boskovic, Switchable cobalt coordination polymers: Spin crossover and valence tautomerism, *Coord. Chem. Rev.*, 2018, **375**, 256–266.

16 I. Krivokapic, M. Zerara, M. L. Daku, A. Vargas, C. Enachescu, C. Ambrus, *et al.*, Spin-crossover in cobalt (II) imine complexes, *Coord. Chem. Rev.*, 2007, **251**, 364–378.

17 R. G. Miller, S. Narayanaswamy, J. L. Tallon and S. Brooker, Spin crossover with thermal hysteresis in cobalt(II) complexes and the importance of scan rate, *New J. Chem.*, 2014, **38**, 1932.

18 P. E. Figgins and D. H. Busch, Complexes of Iron(II), Cobalt(II) and Nickel(II) with Biacetyl-bis-methylimine, 2-Pyridinal-methylimine and 2, 6-Pyridindial-bis-methylimine, *J. Am. Chem. Soc.*, 1960, **82**, 820–824.

19 P. Gütlich and H. Goodwin, *Spin Crossover in Transition Metal Compounds II*, Springer, 2004.

20 S. Kremer, W. Henke and D. Reinen, High-spin-low-spin equilibriums of cobalt(2+) in the terpyridine complexes $Co(terpy)_2X_2{\cdot}nH_2O$, *Inorg. Chem.*, 1982, **21**, 3013–3022.

21 X. Zhang, Z. X. Wang, H. Xie, M. X. Li, T. J. Woods and K. R. Dunbar, A cobalt(II) spin-crossover compound with partially charged TCNQ radicals and an anomalous conducting behavior, *Chem. Sci.*, 2016, **7**, 1569–1574.

22 M. C. Pfrunder, J. J. Whittaker, S. Parsons, B. Moubaraki, K. S. Murray, S. A. Moggach, *et al.*, Controlling Spin Switching with Anionic Supramolecular Frameworks, *Chem. Mater.*, 2020, **32**, 3229–3234.

23 G. Poneti, M. Mannini, L. Sorace, P. Sainctavit, M. A. Arrio, A. Rogalev, *et al.*, X-ray Absorption Spectroscopy as a Probe of Photo- and Thermally Induced Valence Tautomeric Transition in a 1 : 1 Cobalt-Dioxolene Complex, *ChemPhysChem*, 2009, **10**, 2090–2095.

24 M. Graf, G. Wolmershäuser, H. Kelm, S. Demeschko, F. Meyer and H. J. Krüger, Temperature-Induced Spin-Transition in a Low-Spin Cobalt(II) Semiquinonate Complex, *Angew. Chem., Int. Ed.*, 2010, **49**, 950–953.

25 P. Thuery and J. Zarembowitch, Spin state of cobalt(II) in five- and six-coordinate Lewis base adducts of N, N′-ethylenebis(3-carboxysalicylaldiminato)cobalt(II). New spin-crossover complexes, *Inorg. Chem.*, 1986, **25**, 2001–2008.

26 A. Starikov, V. Minkin and A. Starikova, Spin crossover in monoadducts of Co (Salen) with pyridine and imidazole: a quantum chemical study, *Struct. Chem.*, 2014, **25**, 1865–1871.

27 P. Guionneau, M. Marchivie, G. Bravic, J. Letard and D. Chasseau, in *Spin crossover in Transition Metal Compounds II*, ed. P. Gütlich and H. A. Goodwin, Springer, 2004, vol. 234, pp. 97–128.

28 C. Sousa, C. de Graaf, A. Rudavskyi and R. Broer, Theoretical study of the light-induced spin crossover mechanism in $[Fe(mtz)_6]^{2+}$ and $[Fe(phen)_3]^{2+}$, *J. Phys. Chem. A*, 2017, **121**, 9720–9727.

29 G. W. Everett Jr and R. H. Holm, Comparative stereochemical populations and thermodynamics of structural interconversion of planar and tetrahedral cobalt(II) and nickel(II) complexes, *Inorg. Chem.*, 1968, **7**, 776–785.

30 D. H. Gerlach and R. H. Holm, Preparation and stereochemistry of bis-chelate chromium(II), manganese(II), iron(II), and cobalt(II) complexes of the types M-O4 and M-O2S2, *Inorg. Chem.*, 1969, **8**, 2292–2297.

31 J. A. Wolny, M. F. Rudolf, Z. Ciunik, K. Gatner and S. Wołowiec, Cobalt(II) triazene 1-oxide bis (chelates). A case of planar (low spin)–tetrahedral (high spin) isomerism, *J. Chem. Soc., Dalton Trans.*, 1993, 1611–1622.
32 D. R. Eaton, W. D. Phillips and D. J. Caldwell, Configurations and magnetic properties of the nickel(II) aminotroponeimineates, *J. Am. Chem. Soc.*, 1963, **85**, 397–406.
33 G. W. Everett Jr and R. H. Holm, The synthesis and proton resonance study of the solution equilibria of bis (β-ketoamino) nickel(II) complexes, *J. Am. Chem. Soc.*, 1965, **87**, 2117–2127.
34 G. W. Everett Jr and R. H. Holm, Existence of the planar [UNK] tetrahedral equilibrium in solutions of cobalt(II) complexes, *J. Am. Chem. Soc.*, 1965, **87**, 5266–5267.
35 G. W. Everett Jr and R. H. Holm, Studies of the planar-tetrahedral configurational equilibrium in solutions of bis (β-ketoamino) cobalt(II) complexes, *J. Am. Chem. Soc.*, 1966, **88**, 2442–2451.
36 M. Nicolini, C. Pecile and A. Turco, A high spin-low spin conformational equilibrium in the complex dithiocyanato-bis (triethylphosphine) cobalt(II), *Coord. Chem. Rev.*, 1966, **1**, 133–144.
37 C. Daul, S. Niketic, C. Rauzy and C. W. Schläpfer, Polytopal Rearrangement of [Ni(acac)$_2$(py)]: A New Square Pyramid⇄Trigonal Bipyramid Twist Mechanism, *Chem. – Eur. J.*, 2004, **10**, 721–727.
38 A. G. Starikov, R. M. Minyaev and V. I. Minkin, Theoretical modeling of the square-planar to tetrahedral isomerization of bis-chelate nickel(II) complexes, *Chem. Phys. Lett.*, 2008, **459**, 27–32.
39 H. G. Brittain, Proton magnetic resonance spectrum of magnesium acetylacetonate in chloroform-d. Evidence for conformational equilibrium, *Inorg. Chem.*, 1975, **14**, 2858–2860.
40 F. A. Cotton and R. H. Holm, Magnetic investigations of spin-free cobaltous complexes. III. On the existence of planar complexes, *J. Am. Chem. Soc.*, 1960, **82**, 2979–2983.
41 F. A. Cotton and R. H. Soderberg, A Spectroscopic Study of the Polymeric Nature of Bis(acetylacetonato)cobalt(II), *Inorg. Chem.*, 1964, **3**, 1–5.
42 F. A. Cotton and R. C. Elder, The Tetrameric Structure of Anhydrous, Crystalline Cobalt(II) Acetylacetonate, *J. Am. Chem. Soc.*, 1964, **86**, 2294–2295.
43 F. A. Cotton and R. C. Elder, Crystal Structure of Tetrameric Cobalt(II) Acetylacetonate, *Inorg. Chem.*, 1965, **4**, 1145–1151.
44 V. D. Vreshch, J. H. Yang, H. Zhang, A. S. Filatov and E. V. Dikarev, Monomeric Square-Planar Cobalt(II) Acetylacetonate: Mystery or Mistake?, *Inorg. Chem.*, 2010, **49**, 8430–8434.
45 J. Burgess, J. Fawcett, D. R. Russell and S. R. Gilani, Monomeric bis(2,4-pentanedionato)cobalt(II), *Acta Crystallogr., Sect. C:Cryst. Struct. Commun.*, 2000, **56**, 649–650.
46 J. Burgess, J. Fawcett and D. R. Russell, Bis(2, 4-pentanedionato)cobalt(II), *Acta Crystallogr.*, 2011, **67**, e13–e13.
47 P. Pietrzyk, M. Srebro, M. Radoń, Z. Sojka and A. Michalak, Spin Ground State and Magnetic Properties of Cobalt(II): Relativistic DFT Calculations Guided by EPR Measurements of Bis(2, 4-acetylacetonate)cobalt(II)-Based Complexes, *J. Phys. Chem. A*, 2011, **115**, 2316–2324.
48 M. Radoń, M. Srebro and E. Broclawik, Conformational Stability and Spin States of Cobalt(II) Acetylacetonate: CASPT2 and DFT Study, *J. Chem. Theory Comput.*, 2009, **5**, 1237–1244.
49 S. Carlotto, M. Sambi, A. Vittadini and M. Casarin, Theoretical modeling of the $L_{2,3}$-edge X-ray absorption spectra of Mn(acac)$_2$ and Co(acac)$_2$ complexes, *Phys. Chem. Chem. Phys.*, 2016, **18**, 2242–2249.
50 J. Cirera, E. Ruiz and S. Alvarez, Continuous Shape Measures as a Stereochemical Tool in Organometallic Chemistry, *Organometallics*, 2005, **24**, 1556–1562.
51 M. Swart and M. Gruden, Spinning around in Transition-Metal Chemistry, *Acc. Chem. Res.*, 2016, **49**, 2690–2697.
52 S. Roy Chowdhury and S. Mishra, Ab Initio Investigation of Magnetic Anisotropy in Intermediate Spin Iron(III) Complexes, *J. Chem. Phys.*, 2018, **149**, 234302.
53 M. Swart, Accurate Spin-State Energies for Iron Complexes, *J. Chem. Theory Comput.*, 2008, **4**, 2057–2066.
54 M. Pápai, G. Vankó, C. de Graaf and T. Rozgonyi, Theoretical Investigation of the Electronic Structure of Fe (II) Complexes at Spin-State Transitions, *J. Chem. Theory Comput.*, 2013, **9**, 509–519.
55 M. Reiher, Theoretical Study of the Fe(phen)$_2$ (NCS)$_2$ Spin-Crossover Complex with Reparametrized Density Functionals, *Inorg. Chem.*, 2002, **41**, 6928–6935.
56 C. Riplinger and F. Neese, An efficient and near linear scaling pair natural orbital based local coupled cluster method, *J. Chem. Phys.*, 2013, **138**, 034106.
57 C. Riplinger, B. Sandhoefer, A. Hansen and F. Neese, Natural triple excitations in local coupled cluster calculations with pair natural orbitals, *J. Chem. Phys.*, 2013, **139**, 134101.
58 C. Riplinger, P. Pinski, U. Becker, E. F. Valeev and F. Neese, Sparse maps—A systematic infrastructure for reduced-scaling electronic structure methods. II. Linear scaling domain based pair natural orbital coupled cluster theory, *J. Chem. Phys.*, 2016, **144**, 024109.
59 M. Saitow, U. Becker, C. Riplinger, E. F. Valeev and F. Neese, A new near-linear scaling, efficient and accurate, open-shell domain-based local pair natural orbital coupled cluster singles and doubles theory, *J. Chem. Phys.*, 2017, **146**, 164105.
60 Y. Guo, C. Riplinger, U. Becker, D. G. Liakos, Y. Minenkov, L. Cavallo, *et al.*, Communication: An improved linear scaling perturbative triples correction for the domain based local pair-natural orbital based singles and doubles coupled cluster method [DLPNO-CCSD(T)], *J. Chem. Phys.*, 2018, **148**, 011101.
61 B. A. Finney, S. Roy Chowdhury, C. Kirkvold and B. Vlaisavljevich, CASPT2 molecular geometries of Fe(II) spin-crossover complexes, *Phys. Chem. Chem. Phys.*, 2022, **24**, 1390–1398.

62 D. G. Liakos, M. Sparta, M. K. Kesharwani, J. M. L. Martin and F. Neese, Exploring the accuracy limits of local pair natural orbital coupled-cluster theory, *J. Chem. Theory Comput.*, 2015, **11**, 1525–1539.
63 D. G. Liakos and F. Neese, Is it possible to obtain coupled cluster quality energies at near density functional theory cost? Domain-based local pair natural orbital coupled cluster vs modern density functional theory, *J. Chem. Theory Comput.*, 2015, **11**, 4054–4063.
64 S. Roy Chowdhury, N. Nguyen and B. Vlaisavljevich, Importance of Dispersion in the Molecular Geometries of Mn(III) Spin-Crossover Complexes, *J. Phys. Chem. A*, 2023, **127**, 3072–3081.
65 S. Maria, H. Kaneyoshi, K. Matyjaszewski and R. Poli, Effect of Electron Donors on the Radical Polymerization of Vinyl Acetate Mediated by [Co(acac)$_2$]: Degenerative Transfer versus Reversible Homolytic Cleavage of an Organocobalt (III) Complex, *Chem. – Eur. J.*, 2007, **13**, 2480–2492.
66 K. P. Kepp, Theoretical study of spin crossover in 30 iron complexes, *Inorg. Chem.*, 2016, **55**, 2717–2727.
67 K. Pierloot, B. J. Persson and B. O. Roos, Theoretical Study of the Chemical Bonding in [Ni(C_2H_4)] and Ferrocene, *J. Phys. Chem.*, 1995, **99**, 3465–3472.
68 K. Andersson and B. O. Roos, Excitation energies in the nickel atom studied with the complete active space SCF method and second-order perturbation theory, *Chem. Phys. Lett.*, 1992, **191**, 507–514.
69 K. Pierloot, Transition metals compounds: Outstanding challenges for multiconfigurational methods, *Int. J. Quantum Chem.*, 2011, **111**, 3291–3301.
70 S. K. Singh and G. Rajaraman, Deciphering the origin of giant magnetic anisotropy and fast quantum tunnelling in Rhenium (IV) single-molecule magnets, *Nat. Chem.*, 2016, **7**, 10669.
71 A. Sarkar, S. Tewary, S. Sinkar and G. Rajaraman, Magnetic Anisotropy in $Co^{II}X_4$ (X=O, S, Se) Single-Ion Magnets: Role of Structural Distortions versus Heavy Atom Effect, *Chem. – Asian J.*, 2019, **14**, 4696–4704.
72 A. Swain, T. Sharma and G. Rajaraman, Strategies to quench quantum tunneling of magnetization in lanthanide single molecule magnets, *Chem. Commun.*, 2023, **59**, 3206–3228.
73 W. Low, Electronic Phenomenon: Electron Paramagnetic Resonance of Transition Ions. A. Abragam and B. Bleaney. Clarendon (Oxford University Press), New York, 1970. xvi, 912 pp., illus. $41.50. International Series of Monographs on Physics, *Science*, 1971, **171**, 1141–1141.
74 L. Ungur and L. F. Chibotaru, Magnetic anisotropy in the excited states of low symmetry lanthanide complexes, *Phys. Chem. Chem. Phys.*, 2011, **13**, 20086.
75 F. Weigend and R. Ahlrichs, Balanced Basis Sets of Split Valence, Triple Zeta Valence and Quadruple Zeta Valence Quality for H to Rn: Design and Assessment of Accuracy, *Phys. Chem. Chem. Phys.*, 2005, **7**, 3297–3305.
76 F. Weigend and R. Ahlrichs, Balanced basis sets of split valence, triple zeta valence and quadruple zeta valence quality for H to Rn: Design and assessment of accuracy, *Phys. Chem. Chem. Phys.*, 2005, **7**, 3297.
77 J. P. Perdew, Density-functional approximation for the correlation energy of the inhomogeneous electron gas, *Phys. Rev. B: Condens. Matter Mater. Phys.*, 1986, **33**, 8822–8824.
78 A. D. Becke, Density-functional exchange-energy approximation with correct asymptotic behavior, *Phys. Rev. A*, 1988, **38**, 3098–3100.
79 C. Lee, W. Yang and R. G. Parr, Development of the Colle-Salvetti Correlation-Energy Formula into a Functional of the Electron Density, *Phys. Rev. B: Condens. Matter Mater. Phys.*, 1988, **37**, 785–789.
80 J. P. Perdew, J. A. Chevary, S. H. Vosko, K. A. Jackson, M. R. Pederson, D. J. Singh, *et al.*, Atoms, molecules, solids, and surfaces: Applications of the generalized gradient approximation for exchange and correlation, *Phys. Rev. B: Condens. Matter Mater. Phys.*, 1992, **46**, 6671–6687.
81 J. P. Perdew, J. A. Chevary, S. H. Vosko, K. A. Jackson, M. R. Pederson, D. J. Singh, *et al.*, Erratum: Atoms, molecules, solids, and surfaces: Applications of the generalized gradient approximation for exchange and correlation, *Phys. Rev. B: Condens. Matter Mater. Phys.*, 1993, **48**, 4978–4978.
82 A. D. Becke, Density-functional thermochemistry. IV. A new dynamical correlation functional and implications for exact-exchange mixing, *J. Chem. Phys.*, 1996, **104**, 1040–1046.
83 A. D. Becke, Density-functional thermochemistry. V. Systematic optimization of exchange-correlation functionals, *J. Chem. Phys.*, 1997, **107**, 8554–8560.
84 C. Adamo and V. Barone, Toward reliable density functional methods without adjustable parameters: The PBE0 model, *J. Chem. Phys.*, 1999, **110**, 6158–6170.
85 T. Yanai, D. P. Tew and N. C. Handy, A New Hybrid Exchange-Correlation Functional Using the Coulomb-Attenuating Method (CAM-B3LYP), *Chem. Phys. Lett.*, 2004, **393**, 51–57.
86 M. Reiher, O. Salomon and B. A. Hess, Reparameterization of hybrid functionals based on energy differences of states of different multiplicity, *Theor. Chem. Acc.*, 2001, **107**, 48–55.
87 V. N. Staroverov, G. E. Scuseria, J. Tao and J. P. Perdew, Comparative assessment of a new nonempirical density functional: Molecules and hydrogen-bonded complexes, *J. Chem. Phys.*, 2003, **119**, 12129–12137.
88 Y. Zhao, N. E. Schultz and D. G. Truhlar, Design of Density Functionals by Combining the Method of Constraint Satisfaction with Parametrization for Thermochemistry, Thermochemical Kinetics, and Noncovalent Interactions, *J. Chem. Theory Comput.*, 2006, **2**, 364–382.
89 Y. Zhao and D. G. Truhlar, The M06 suite of density functionals for main group thermochemistry, thermochemical kinetics, noncovalent interactions, excited states, and transition elements: two new functionals and systematic testing of four M06-class functionals and 12 other functionals, *Theor. Chem. Acc.*, 2007, **120**, 215–241.

90 S. Grimme, Semiempirical hybrid density functional with perturbative second-order correlation, *J. Chem. Phys.*, 2006, **124**, 034108.
91 S. Grimme, J. Antony, S. Ehrlich and H. Krieg, A consistent and accurate ab initio parametrization of density functional dispersion correction (DFT-D) for the 94 elements H-Pu, *J. Chem. Phys.*, 2010, **132**, 154104.
92 S. Grimme, S. Ehrlich and L. Goerigk, Effect of the damping function in dispersion corrected density functional theory, *J. Comput. Chem.*, 2011, **32**, 1456–1465.
93 J. N. Harvey, M. Aschi, H. Schwarz and W. Koch, The singlet and triplet states of phenyl cation. A hybrid approach for locating minimum energy crossing points between non-interacting potential energy surfaces, *Theor. Chem. Acc.*, 1998, **99**, 95–99.
94 Y. Shiota, D. Sato, G. Juhasz and K. Yoshizawa, Theoretical Study of Thermal Spin Transition between the Singlet State and the Quintet State in the $[Fe(2\text{-picolylamine})_3]^{2+}$ Spin Crossover System, *J. Phys. Chem. A*, 2010, **114**, 5862–5869.
95 K. V. Bozhenko, A. N. Utenyshev, A. A. Starikova, A. V. Metelitsa, A. G. Starikov, V. I. Minkin, *et al.*, Computational insight into spatial and electronic structure of bis-diketonate cobalt complexes with triphenodioxazine ligands, *Chem. Phys. Lett.*, 2023, **813**, 140286.
96 M. J. Frisch, G. W. Trucks, H. B. Schlegel, G. E. Scuseria, M. A. Robb and J. R. Cheeseman, et al., *Gaussian16 Revision C.01*, 2016, Gaussian Inc., Wallingford CT.
97 D. G. Liakos, M. Sparta, M. K. Kesharwani, J. M. L. Martin and F. Neese, Exploring the Accuracy Limits of Local Pair Natural Orbital Coupled-Cluster Theory, *J. Chem. Theory Comput.*, 2015, **11**, 1525–1539.
98 D. G. Liakos and F. Neese, Is It Possible To Obtain Coupled Cluster Quality Energies at near Density Functional Theory Cost? Domain-Based Local Pair Natural Orbital Coupled Cluster vs Modern Density Functional Theory, *J. Chem. Theory Comput.*, 2015, **11**, 4054–4063.
99 C. Riplinger and F. Neese, An efficient and near linear scaling pair natural orbital based local coupled cluster method, *J. Chem. Phys.*, 2013, **138**, 034106.
100 C. Riplinger, B. Sandhoefer, A. Hansen and F. Neese, Natural triple excitations in local coupled cluster calculations with pair natural orbitals, *J. Chem. Phys.*, 2013, **139**, 134101.
101 N. B. Balabanov and K. A. Peterson, Systematically convergent basis sets for transition metals. I. All-electron correlation consistent basis sets for the 3d elements Sc-Zn, *J. Chem. Phys.*, 2005, **123**, 064107.
102 N. B. Balabanov and K. A. Peterson, Basis set limit electronic excitation energies, ionization potentials, and electron affinities for the 3d transition metal atoms: Coupled cluster and multireference methods, *J. Chem. Phys.*, 2006, **125**, 074110.
103 G. L. Stoychev, A. A. Auer and F. Neese, Automatic Generation of Auxiliary Basis Sets, *J. Chem. Theory Comput.*, 2017, **13**, 554–562.
104 P. Comba, D. Faltermeier, S. Krieg, B. Martin and G. Rajaraman, Spin state and reactivity of iron(IV) oxido complexes with tetradentate bispidine ligands, *Dalton Trans.*, 2020, **49**, 2888–2894.
105 S. Sharma, B. Pandey and G. Rajaraman, The interplay of covalency, cooperativity, and coupling strength in governing C–H bond activation in Ni_2E_2 (E = O, S, Se, Te) complexes, *Chem. Sci.*, 2024, **15**, 10529–10540.
106 T. J. Lee and P. R. Taylor, A diagnostic for determining the quality of single-reference electron correlation methods, *Int. J. Quantum Chem.*, 2009, **36**, 199–207.
107 B. O. Roos, P. R. Taylor and P. E. M. Sigbahn, A complete active space SCF method (CASSCF) using a density matrix formulated super-CI approach, *Chem. Phys.*, 1980, **48**, 157–173.
108 B. O. Roos, The complete active space SCF method in a fock-matrix-based super-CI formulation, *Int. J. Quantum Chem.*, 2009, **18**, 175–189.
109 C. Angeli, R. Cimiraglia, S. Evangelisti, T. Leininger and J.-P. Malrieu, Introduction of n-electron valence states for multireference perturbation theory, *J. Chem. Phys.*, 2001, **114**, 10252–10264.
110 C. Angeli, R. Cimiraglia and J. P. Malrieu, N-electron valence state perturbation theory: a fast implementation of the strongly contracted variant, *Chem. Phys. Lett.*, 2001, **350**, 297–305.
111 C. Angeli, R. Cimiraglia and J. P. Malrieu, n-electron valence state perturbation theory: A spinless formulation and an efficient implementation of the strongly contracted and of the partially contracted variants, *J. Chem. Phys.*, 2002, **117**, 9138–9153.
112 C. Angeli, S. Borini, M. Cestari and R. Cimiraglia, A quasidegenerate formulation of the second order n-electron valence state perturbation theory approach, *J. Chem. Phys.*, 2004, **121**, 4043–4049.
113 S. K. Singh, J. Eng, M. Atanasov and F. Neese, Covalency and chemical bonding in transition metal complexes: An ab initio based ligand field perspective, *Coord. Chem. Rev.*, 2017, **344**, 2–25.
114 D. M. P. Mingos, P. Day and J. P. Dahl, *Molecular electronic structures of transition metal complexes II*, Springer Science and Business Media, 2012, vol. 2.
115 P. Å. Malmqvist and B. O. Roos, The CASSCF state interaction method, *Chem. Phys. Lett.*, 1989, **155**, 189–194.
116 L. F. Chibotaru and L. Ungur, Ab initio calculation of anisotropic magnetic properties of complexes. I. Unique definition of pseudospin Hamiltonians and their derivation, *J. Chem. Phys.*, 2012, **137**, 064112.
117 F. Neese, Software update: The ORCA program system—Version 5.0, *Wiley Interdiscip. Rev.: Comput. Mol. Sci.*, 2022, **12**, e1606.
118 F. Neese, F. Wennmohs, U. Becker and C. Riplinger, The ORCA quantum chemistry program package, *J. Chem. Phys.*, 2020, **152**, 224108.
119 F. Neese, The ORCA program system, *Wiley Interdiscip. Rev.: Comput. Mol. Sci.*, 2011, **2**, 73–78.

